

Soft Matter

Accepted Manuscript



This is an *Accepted Manuscript*, which has been through the Royal Society of Chemistry peer review process and has been accepted for publication.

Accepted Manuscripts are published online shortly after acceptance, before technical editing, formatting and proof reading. Using this free service, authors can make their results available to the community, in citable form, before we publish the edited article. We will replace this *Accepted Manuscript* with the edited and formatted *Advance Article* as soon as it is available.

You can find more information about *Accepted Manuscripts* in the [Information for Authors](#).

Please note that technical editing may introduce minor changes to the text and/or graphics, which may alter content. The journal's standard [Terms & Conditions](#) and the [Ethical guidelines](#) still apply. In no event shall the Royal Society of Chemistry be held responsible for any errors or omissions in this *Accepted Manuscript* or any consequences arising from the use of any information it contains.

Effect of Interface Shape on Advancing and Receding Fluid-Contact Angles around Spherical Particles

Nesrin Şenbil, Wei He, Vincent Démery, Anthony D. Dinsmore*

Department of Physics, Univ. of Massachusetts Amherst, MA 01003

*Email: dinsmore@physics.umass.edu

ABSTRACT: The angle of contact between a solid surface and a fluid interface plays a key role in wetting and is therefore a focus in studies of a wide range of natural phenomena and fluidic technologies. The contact angle ranges between two values, a maximum (advancing) angle and a minimum (receding) angle. These limiting angles are thought to be properties of the fluids and of the chemistry or topography of the solid. By contrast, we find that the value of the receding angle can be significantly reduced by altering the interface shape. Using millimeter-sized spheres coated with polydimethylsiloxane and pulled through an air-water interface, we observe that the receding angle decreases from $101 \pm 1^\circ$ at a planar interface to as low as $80 \pm 1^\circ$ at saddle- or cylinder-shaped interfaces. The angle decreases smoothly with the deviatoric curvature of the interface (a measure of the shape anisotropy) and is linked to a non-circular contact line.

Contacts between fluid interfaces and solid surfaces arise in diverse settings ranging from water droplets condensing on a surface to particles coating oil droplets in water¹⁻⁵. The contact angle, θ , between the interface and the solid plays the key role in determining the droplet shape and stability, which are essential in applications such as water-repellant surfaces or Pickering emulsions in the food or oil-recovery industries⁶⁻¹⁰. In contrast to Young's equilibrium prediction^{2, 5}, experiments routinely show a range of θ values in steady state, ranging between a maximum (θ_A) when the fluid advances over a non-wet substrate and a minimum (θ_R) when it recedes^{1, 11}. This hysteresis is attributed to a variety of mechanisms that are intrinsic to the materials¹²⁻¹⁶ or involve dissipation^{16,17}, heterogeneities^{1, 5, 18}, surface topography^{2, 5, 10} or a three-phase line tension^{1, 5, 19}. In these models¹¹, it is assumed that $\theta_{R,A}$ are a property of the two fluids and the solid surface. Here we show, by contrast, that the receding angle θ_R can be substantially reduced by tuning the shape of the fluid interface. We measured θ_R around a millimeter-scale sphere at an air-water interface and found $\theta_R = 101 \pm 1^\circ$ at an initially planar interface, and θ_R as low as $80 \pm 1^\circ$ at saddle- and cylinder-shaped interfaces. θ_R decreased monotonically with increasing deviatoric curvature (shape anisotropy) of the interface and correlated with undulation of the contact line. In these same interfaces, θ_A remained unchanged. Our results pave the way to new fundamental insights and improvements in wetting-based materials for icephobic, self-drying, self-cleaning or water-harvesting applications and for particle-stabilized emulsions^{3, 10, 20-24}.

We used millimeter-scale glass spheres of radius $a = 1.6$ and 1.2 mm, which were cleaned in Nochromix® and sulfuric acid, thoroughly rinsed, and then chemically modified with polydimethylsiloxane (trimethylsiloxy terminated PDMS, 94 kDa; Gelest cat no. DMS-T22) to yield smooth contact lines [see online supplementary materials for details and for

AFM measurements (Fig. S1)]. Each sphere was attached to a rigid rod that was clamped to a translation stage, so that the sphere could be moved vertically through the interface [Fig. 1(a)]. A typical experiment started with the dry sphere in air. The sphere was displaced downward into the water in increments of 0.2 mm, during which process the contact line advanced across the dry sphere. After the sphere was fully immersed, we then displaced it upward in increments of 0.2 mm until it detached from the interface. After each displacement, we waited 5 s for the flow to cease, then acquired an image of the cross-section of the interface in the plane that includes the center of the sphere [Fig. 1(c)]. In experiments with two spheres (described below), the centers of both spheres lay in the image plane so that the interface shape should have reflection symmetry about the image plane.

Images of the spheres and interface were obtained using a Nikon D5100 digital camera with a 60 mm lens and 68 mm of extension tubes. The depth L_D , defined as the distance between the undisturbed interface and the bottom of the sphere, was obtained from the images. The sphere, the air-water interface, and the contact line were imaged with a resolution of approx. 5 μm . With our methods, we are able to measure the contact angles at the left and right sides of the imaged plane only [Figure 3]. Contact angles on the left and right sides of the target sphere were obtained by two methods. In one method (referred to as ‘geometric’), we first drew a circle on top of the glass sphere using ImageJ²⁵, then drew a line tangent to the sphere where it met the interface. We then identified the air-water interface by eye and used the ImageJ angle-measuring tool to find θ . Error bars were estimated by analyzing the same image three times. To test left-right measurement bias, we repeated the analysis after reflecting images about the vertical axis and found no systematic difference. As an alternative method, we extracted the shape of the interface from the image and fit these data to a functional form that includes a logarithmic deformation centered on each sphere plus a quadrupolar deformation that decays with the inverse square of distance. We obtained good agreement with the data [Supplementary Information]. From the best-fit parameters, we calculated the slope of the interface at the contact point, and then found the angle θ between the interface and the tangent to the particle. These two methods agreed with each other within uncertainties [Supplementary Information, Fig. S3]. For the remainder of this manuscript, we report the contact angles as measured by the more straightforward geometric method.

Figure 2 shows the measured θ vs. immersion depth L_D in a typical experiment in which the interface was initially planar. The plot shows a consistent angle in the pushing-down process, during which the contact line advanced across the dry particle surface. The average of these measurements is the apparent advancing angle, $\theta_A = 109 \pm 1^\circ$. During the pulling-up (receding contact) process, we found that θ initially decreased and then remained unchanged within our precision as L_D was changed by 2-3 mm. The average of these latter pulling-up measurements is the apparent receding angle, $\theta_R = 101 \pm 1^\circ$. We detected no variation in θ from run to run, nor a difference between left and right sides, nor variation of θ with displacement once the contact line was fully receding or advancing [Fig. 2(a)]. We found no time evolution of θ over a period of 300 s following displacement [Fig. 2(b)]; in particular, we did not find the logarithmic aging that was reported for microspheres and attributed to contact-line pinning²⁶. All of these results are consistent with the known phenomenon of contact-angle hysteresis.

We now turn to θ measurements when the interface was non-planar. We used two types of anisotropic shapes: saddle and cylindrical. To make the interface saddle-like, we inserted a secondary glass sphere partway into the interface [Fig. 3]. Once this sphere was in place, the sphere that had been used in the initial flat-interface measurement (the ‘target’ sphere) was pushed through the interface nearby, following the same procedure as for Fig. 2. The secondary glass sphere that we used to alter the interface shape was either PDMS-coated like the target sphere [Fig. 3(c)], or washed with KOH to make it hydrophilic [Fig. 3(d)]. Purpose of using hydrophobic or hydrophilic secondary spheres is to check affect of anisotropy in opposite directions. To make the interface cylindrical in shape, we confined it between two parallel razor blades (for \cap -shaped curvature) or between two hydrophilic, KOH-washed glass slides (for \cup -shaped curvature).

The vertical axis of Fig. 4(a) shows the measured θ_R for the target sphere at saddle and cylindrical interfaces. We always compare θ_R of the same target sphere at the initially planar and curved interfaces. We thus keep the surface properties constant and tune only the shape of the liquid interface. In each case, the target sphere had been pulled upward prior to the measurement, so that the interface was fully receding. For all of the spheres used in Fig. 4, we verified that θ_R at the planar interface was $101 \pm 1^\circ$. Contact angles were measured with both the geometric and fitting methods as described earlier. Our results show that θ_R decreased by as much as 11° for the 1.6-mm-radius sphere at a saddle-like interface, and by as much as 21° for a 1.2-mm-radius sphere at a cylindrical interface.

For all of these experiments, θ_A was indistinguishable from the planar-interface experiment ($\theta_A = 109 \pm 1^\circ$). Aside from highlighting a distinction between advancing and receding, this result also shows that the change of θ_R was not an image artifact arising from curvature (which, if present, should also affect θ_A). Furthermore, these θ_R results are repeatable: at saddle interfaces after we removed the secondary sphere, the interface returned to a planar shape and a measurement of the hysteresis loop was indistinguishable from the first trace (stars in Fig. 2(b)).

To identify how interface shape is related to the reduction of θ_R , we first note that the planar interface data show that θ_R is unaffected by the interface slope and mean curvature at the contact (which both vary with L_D), so these parameters cannot be the essential ones. Instead, we find that anisotropy of the interface shape correlates most strongly with the drop in θ_R . Shape anisotropy is characterized by the deviatoric curvature (D): if we define c_1 and c_2 as the two principal curvatures of the interface, then $D \equiv (c_1 - c_2)/2$, where c_1 lies in the image plane and is defined positive for upward curvature. Hence $D = 0$ for isotropic shapes such as planes and spheres and $D \neq 0$ for cylinders or saddles. Here, D_0 characterizes the initial interface anisotropy prior to insertion of the target sphere. For cylindrical interfaces, D_0 is simply $\frac{1}{2}$ the curvature of the cylinder, obtained from images. For saddle-shaped interfaces, we measured D_0 at a symmetric position on the opposite side of the secondary sphere [inset of Fig. 4(a)]. The in-plane curvature c_1 was obtained from the image and c_2 was obtained by balancing Laplace pressure and gravitational pressure; see supplementary materials for details].

Figure 4 shows a plot of the measured receding angle θ_R vs. the absolute value $|D_0|$. We have expressed $|D_0|$ in a dimensionless form by multiplying by the sphere radius a . The results show a strong correlation: as $a|D_0|$ increased from 0 to approximately 0.3, θ_R smoothly decreased by 21° .

Our results were confirmed for different sizes of spheres, and at both saddle-like and cylindrical interfaces, repeatedly. These angles were measured at the left and right sides of the sphere when we imaged a plane with front-back reflection symmetry; these contact angles on the left and right sides were indistinguishable. One might ask what happens to the contact angle at the other points around the sphere. By imaging cross sections, we cannot accurately measure the contact angle at arbitrary points even when we rotate our camera, because the contact line is not always normal to the image plane, and hence the two rays that define θ do not always lie in the image plane. However, owing to the fact that the cylindrical interface has two perpendicular planes with reflection symmetry, we were able to measure θ along the two axial directions and the two azimuthal directions (the principal curvature directions). We found no difference among these four angles. We also found that the sign of D_0 did not affect the result on saddle-shaped interfaces: when $aD_0 \approx \pm 0.08$, θ_R was approximately 95° for both signs (Fig. 4(a)). Changing the sign of D_0 is equivalent to switching c_1 for c_2 , which is equivalent to a 90° rotation about the \mathbf{z} -axis; hence the irrelevance of the sign implies that θ_R should be the same along the two principal directions, as we found for the cylindrical interface.

In a more extreme case, we brought the sphere into contact with one wall so that it strongly perturbed the interface; in this case we found θ_R as low as 45° (Fig. 3e). Because we could only see one side of the sphere, however, we did not include this data on the plot.

The deviatoric curvature deforms the shape of the contact line itself, which may explain its effect on θ_R . Whereas a sphere pulled from an initially planar interface adopts a circular ring of contact, we find an undulating, non-planar contact line when $D_0 \neq 0$ (Fig. 3(d)). We used ImageJ to extract the projection of the contact line onto the image plane, and then reconstructed the three-dimensional coordinates using the known size and location of the target sphere²⁵ [Supplementary Information]. We parameterize the height, z , of the contact line using a multipole expansion where z_0 is the mean height, z_1 is the tilt relative to the xy plane, z_2 is the undulation with quadrupolar ($\cos(2\phi)$) form, etc., as illustrated in the inset of Fig. 4(b). Here, ϕ is polar angle in the plane of the interface with the sphere at the origin.

Figure 4(b) shows that the quadrupolar component of the contact-line shape is approximately proportional to D_0 . (For z_1 , z_3 , etc, see Fig. S4.) This undulation can be understood as a consequence of the interface shape anisotropy: when the sphere is placed at the interface, θ_R must differ along the directions of the two principal curvatures when $c_1 \neq c_2$. Non-uniformity of the contact angle should induce forces that deform the interface until it reaches a steady state. Previous calculations started from the assumption that θ is the Young-Dupre value and that the net force on the sphere is zero (neither of which is the case in our experiment); they predicted that the deformation should have quadrupolar symmetry with amplitude $z_2/a \propto aD_0$ and should decay with the inverse square of distance²⁷⁻²⁹. The scaling of measured z_2/a with aD_0 agrees with this prediction (Fig. 4(b)) and the $1/(\text{distance})^2$ scaling matches our fits to the interface shape [Supplementary Information]. Because θ_R should depend only on forces acting very near the contact line, we propose that the shape of the contact line is the essential factor, and that D_0 plays the role of perturbing the contact-line shape.

Why would the shape of the contact line affect the receding angle and not the advancing angle? First, we note that our results cannot be explained by a three-phase line

tension (energy per unit length of the contact line). A line tension could change the contact angle^{1, 5, 15, 19} by contributing a radially inward or outward force on the contact line, proportional to contact-line curvature. This effect would be visible in the planar-interface data: as the contact ring moves from the upper to the lower half of the sphere, the direction of the contact-line-curvature force should be toward the upper phase and then toward the lower phase (or vice versa), so that θ_R should change. We do not observe such a result.

We can also rule out the possibility that the change in receding angle is due to an irreversible energy cost per area, Γ_R , required to dehydrate a unit area of solid surface and allow the line to recede⁵. Indeed, a straightforward energy argument shows that the receding contact angle would be given by $\cos\theta_R = \cos\theta_{VD} + \Gamma_R/\gamma$, independent of the contact line geometry. This is not consistent with our experimental data.

Our results suggest that the interface shape anisotropy induces a force on the contact line that does not come from interfacial tension, line tension, or local dissipative processes. Since the advancing angle θ_A is not affected by interface shape, this force does not affect the advancing contact line, indicating a significant difference between the advancing and receding contact lines.

In summary, we found that an anisotropically-shaped fluid interface with either saddle or cylindrical shape leads to substantially smaller receding angles on a solid sphere. The receding angle decreased from 101° to 80° when the initial deviatoric curvature changed from $D_0 = 0$ to 0.26 mm^{-1} . The advancing angle remained constant ($109 \pm 1^\circ$), which shows that the change of angle arises from the receding process itself rather than an optical artifact. Aside from the change in the receding contact angle, the interface anisotropy also induces a quadrupolar deformation of the contact line, which we find to be proportional to aD_0 . To our knowledge, this is the first report of a reduction of θ_R arising purely from the shape of the contact line or interface, and we are not aware of any theory that explains it. This result may shed light on the origin of the hysteresis. It may also be that other particle shapes or surface chemistry will show different sensitivity to interface curvature, or that a droplet on a smooth solid surface with $D \neq 0$ will also show a reduced θ_R and provide a new mechanism to optimize materials for droplet nucleation, evaporation, adhesion or motion on surfaces.

Acknowledgments:

This research was made possible in part by a grant from BP/The Gulf of Mexico Research Initiative through the C-MEDS consortium, and in part by the National Science Foundation (CBET-0967620). We thank Ramesh Adhikari for assistance with the AFM, Joseph Krumpfer for assistance with the PDMS, and Benny Davidovitch for helpful discussions.

References

1. de Gennes, P.G. Wetting - Statics and Dynamics. *Rev. Mod. Phys.* **57**, 827-863 (1985).
2. Quere, D. Non-sticking drops. *Rep. Prog. Phys.* **68**, 2495-2532 (2005).
3. Nosonovsky, M. & Bhushan, B. Superhydrophobic surfaces and emerging applications: Non-adhesion, energy, green engineering. *Curr. Opin. Colloid Interface Sci.* **14**, 270-280 (2009).
4. Gao, X.F. & Jiang, L. Water-repellent legs of water striders. *Nature* **432**, 36-36 (2004).

5. Bonn, D., Eggers, J., Indekeu, J., Meunier, J. & Rolley, E. Wetting and spreading. *Rev. Mod. Phys.* **81**, 739-805 (2009).
6. Saha, A., Nikova, A., Venkataraman, P., John, V.T. & Bose, A. Oil Emulsification Using Surface-Tunable Carbon Black Particles. *ACS Appl. Mater. Interfaces* **5**, 3094-3100 (2013).
7. Zhang, H.P. et al. Investigation of OMA formation and the effect of minerals. *Mar. Pollut. Bull.* **60**, 1433-1441 (2010).
8. Paunov, V.N. et al. Emulsions stabilised by food colloid particles: Role of particle adsorption and wettability at the liquid interface. *J. Colloid Interface Sci.* **312**, 381-389 (2007).
9. Binks, B.P. & Murakami, R. Phase inversion of particle-stabilized materials from foams to dry water. *Nat. Mater.* **5**, 865-869 (2006).
10. Furstner, R., Barthlott, W., Neinhuis, C. & Walzel, P. Wetting and self-cleaning properties of artificial superhydrophobic surfaces. *Langmuir* **21**, 956-961 (2005).
11. Eral, H.B., t Mannelje, D. & Oh, J.M. Contact angle hysteresis: a review of fundamentals and applications. *Colloid. Polym. Sci.* **291**, 247-260 (2013).
12. Gregg, S.J. Hysteresis of the Contact Angle. *J. Chem. Phys.* **16**, 549-550 (1948).
13. Extrand, C.W. & Kumagai, Y. An experimental study of contact angle hysteresis. *J. Colloid Interface Sci.* **191**, 378-383 (1997).
14. Chen, Y.L., Helm, C.A. & Israelachvili, J.N. Molecular Mechanisms Associated with Adhesion and Contact-Angle Hysteresis of Monolayer Surfaces. *J. Phys. Chem.* **95**, 10736-10747 (1991).
15. Lam, C.N.C., Wu, R., Li, D., Hair, M.L. & Neumann, A.W. Study of the advancing and receding contact angles: liquid sorption as a cause of contact angle hysteresis. *Adv. Colloid Interface Sci.* **96**, 169-191 (2002).
16. Yang, X.F. Equilibrium Contact-Angle and Intrinsic Wetting Hysteresis. *Appl. Phys. Lett.* **67**, 2249-2251 (1995).
17. Freund, J.B. The atomic detail of a wetting/de-wetting flow. *Phys. Fluids* **15**, L33-L36 (2003).
18. Extrand, C.W. Contact Angles and Hysteresis on Surfaces with Chemically Heterogeneous Islands. *Langmuir* **19**, 3793-3796 (2003).
19. Tadmor, R. Line energy and the relation between advancing, receding, and young contact angles. *Langmuir* **20**, 7659-7664 (2004).
20. Blosssey, R. Self-cleaning surfaces - virtual realities. *Nat. Mater.* **2**, 301-306 (2003).
21. Ju, J. et al. A multi-structural and multi-functional integrated fog collection system in cactus. *Nat. Commun.* **3**, 6 (2012).
22. Grunze, M. Surface science - Driven liquids. *Science* **283**, 41-42 (1999).
23. Jung, S., Tiwari, M.K., Doan, N.V. & Poulikakos, D. Mechanism of supercooled droplet freezing on surfaces. *Nat. Commun.* **3**, 8 (2012).
24. Kulinich, S.A.a.F.M. Effect of contact angle hysteresis on water droplet evaporation from superhydrophobic surfaces. *Appl. Surf. Sci.* **255**, 4056-4060 (2009).
25. Rasband, W.S. (U. S. National Institutes of Health, Bethesda, Maryland, USA, 1997-2011).
26. Kaz, D.M., McGorty, R., Mani, M., Brenner, M.P. & Manoharan, V.N. Physical ageing of the contact line on colloidal particles at liquid interfaces. *Nat. Mater.* **11**, 138-142 (2011).
27. Wurger, A. Curvature-induced capillary interaction of spherical particles at a liquid interface. *Phys. Rev. E* **74**, 041402 (2006).
28. Zeng, C., Brau, F., Davidovitch, B. & Dinsmore, A.D. Capillary Interactions among Spherical Particles at Curved Liquid Interfaces. *Soft Matter* **8**, 8582-8594 (2012).
29. Ershov, D., Sprakel, J., Appel, J., Stuart, M.A.C. & van der Gucht, J. Capillarity-induced ordering of spherical colloids on an interface with anisotropic curvature. *PNAS* **110**, 9220-9224 (2013).

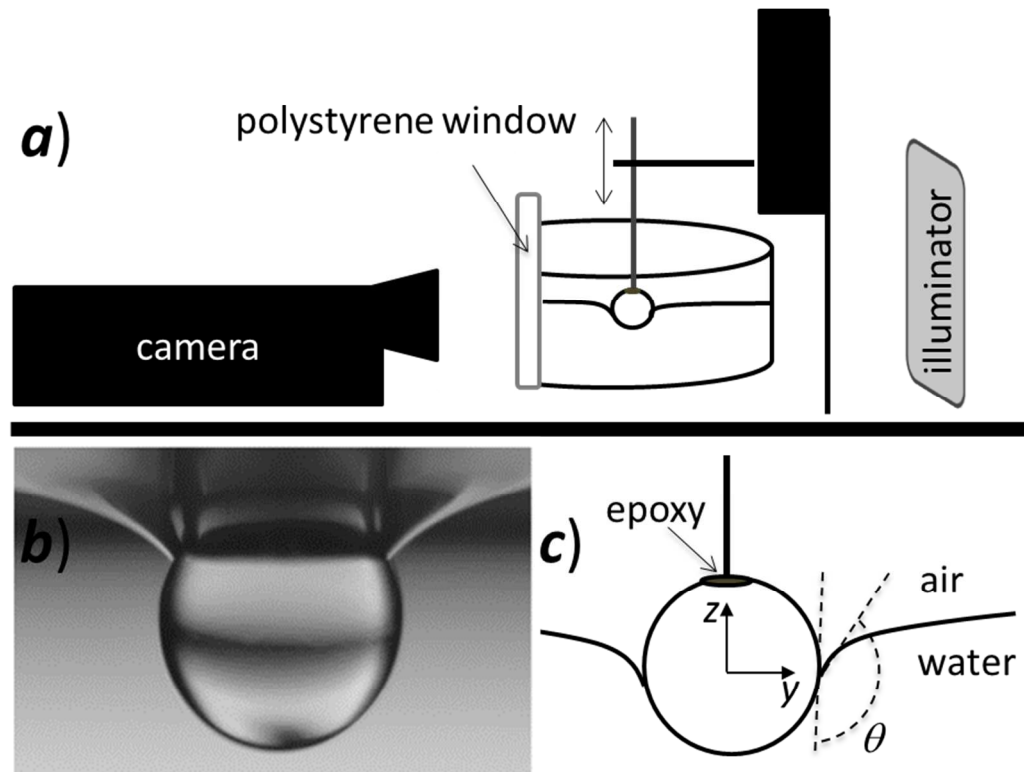


Fig. 1 Experimental setup. **(a)** Schematic of the experiment. A circular polystyrene container is cut on the camera side and a polystyrene slide is attached as a window to avoid refraction at the circular edge. **(b)** Real image (converted to grayscale) of a PDMS coated sphere receding from water after being fully immersed. The contact angle θ is the same on left and right sides and the contact line is smooth. **(c)** The contact angle of a sphere with the interface of water/air is defined as the angle, as measured through the water phase, between the tangent to sphere's surface and the tangent to the interface.

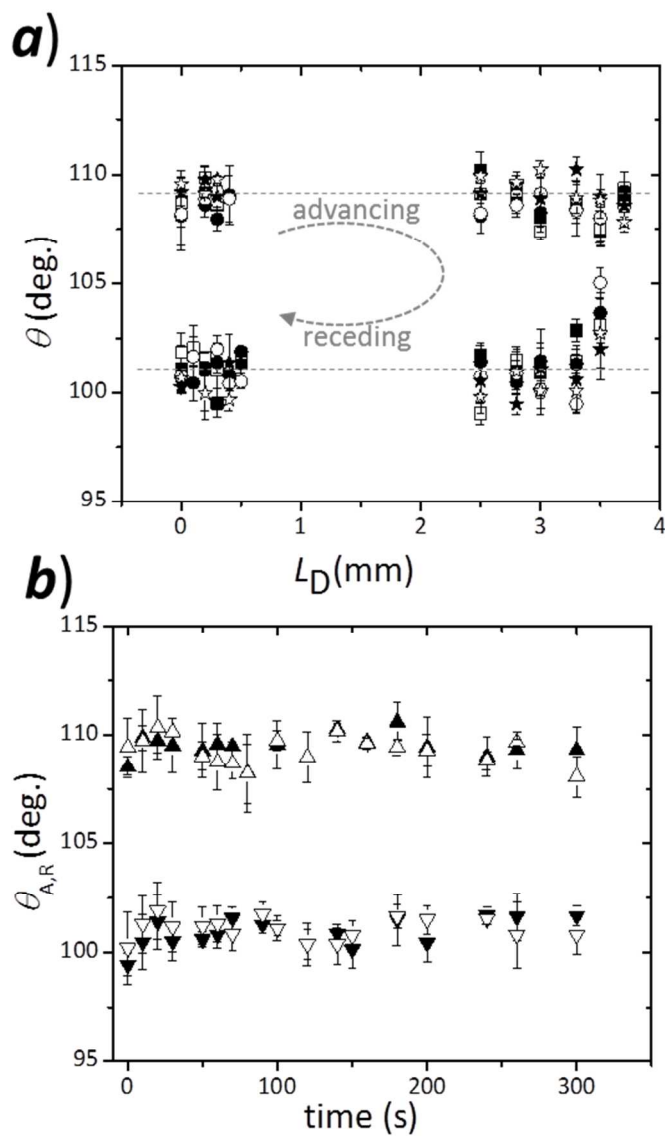


Fig. 2 Contact angles θ at an initially flat interface. **(a)** Contact angles of left and right sides of the same sphere, measured as the sphere was lowered from air ($L_D=0$) into water (advancing contact) and then raised (receding contact). Open (filled) symbols show the left (right) side of the sphere. The first two cycles (squares and circles) were taken one after the other. The third data set (stars) was taken after the experiments shown in Figs. 2(b) and 4. **(b)** Time evolution of θ_A (upper trace) and θ_R (lower trace).

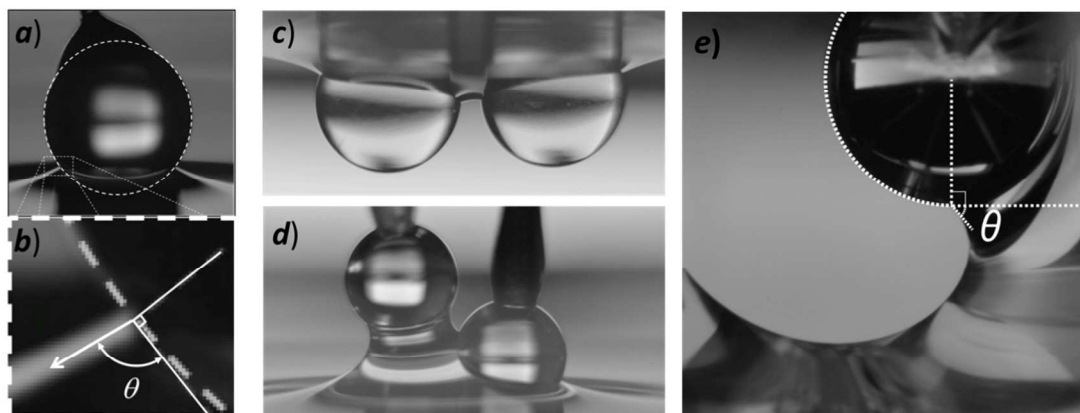


Fig. 3 Raw images at flat and curved interfaces. **(a)** Image of a single sphere following an upward displacement through the interface (*i.e.* receding contact). **(b)** Magnified view, showing how the contact angle θ is measured. **(c)** Image of two spheres at the interface. The target sphere (on the right) is the same as in **(a)** and is receding; the left sphere is hydrophobic (PDMS-coated). **(d)** Image of a target sphere (on the right side) near a hydrophilic sphere, which yields an interface that is more strongly curved and more anisotropic than in **(c)**. A non-planar contact line is visible. **(e)** In this highly curved cylindrical interface case, θ_r is approx. 45° by repeated measurements. (θ_r was 101° at an initially planar liquid interface.)

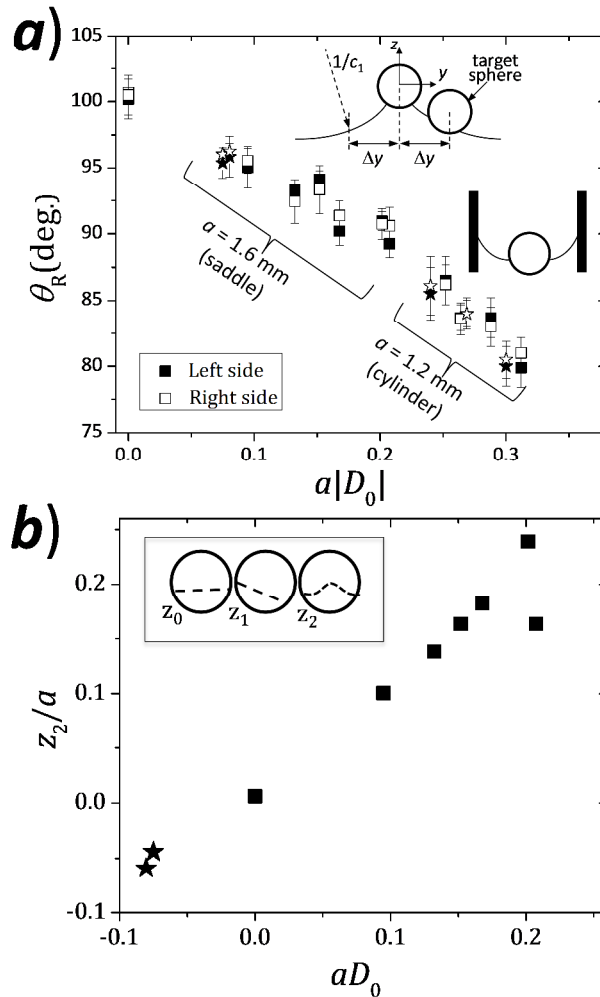


Fig. 4 Comparison of receding angles θ_R and contact-line shapes at different curved interfaces. **(a)** Measured θ_R vs. absolute value of the measured deviatoric curvature D_0 (interface shape anisotropy) multiplied by sphere radius a . $D_0=0$ corresponds to the initially planar interface. \blacksquare : $D_0 \geq 0$; \star : $D_0 < 0$. θ_A remained unchanged in all these experiments. **(Inset)** Illustrations of the saddle and cylindrical interfaces for $D_0 \neq 0$. **(b)** The dimensionless quadrupole component, z_2/a , of the contact-line height plotted against dimensionless deviatoric curvature $D_0 a$ (only data for $a = 1.6$ mm are shown). **(Inset)** Illustration of tilt (z_1) and quadrupolar (z_2) undulations around the sphere.